Adaptive Neuro-Fuzzy Interface System-based SMO for Solar PV Array fed Encoder less PMSM Drive for Irrigation Applications

Rayapati Devi Prasad[1], Dr. A. Hemasekhar[2]

M.Tech Student[1], Professor & HOD[2]

Department of Electrical and Electronics Engineering, VEMU Institute of Technology, P. Kothakota , Andhra Pradesh, India

ABSTRACT

This research work proposes an adaptive neuro-fuzzy interface system based SMO for encoder-less solar PV array PMSM drive for irrigation applications. The PMSM motor is employed and operated for Solar Water Pump System. A new technique named Adaptive Hybrid generalized integrator is employed to overcome the problems like reduced accuracy, sensitive to electromagnetic noise and temperature. In this AHGI based Sliding mode observer PI controller is implemented to regulate the voltage. But using of PI controller will leads system's slow system response time and efficiency of the system will decreases. So, in order to overcome this issues PI controller is replaced with Adaptive neuro-Fuzzy Interface System (ANFIS). For this process, a solar PV is assumed with the incremental conductance based MPPT technique to supply power to the PMSM drive. The supply from the PV will be in the form of DC but the PMSM drive needs AC supply. In order to convert DC electricity to AC power, an inverter is used. The speed and reference speed is considered to generate the reference current. For this regulation AHGI based SMC is employed which is equipped with ANFIS controller is proposed. The ANFIS controller will have high speed response of the system and reduces the harmonic distortions to provide magnified power to the irrigation applications. Using the Matlab/Simulink 2018a software, the performance of the suggested system is assessed.

Keywords : ANFIS Controller, PI Controller, PMSM Drive, Solar PV, Sliding mode control, Inverter, Incremental conductance based MPPT.

I. INTRODUCTION

One of the most important renewable energies is solar photovoltaic (SPV) energy, which is now frequently utilised in systems for distributed generating. The rapid advancement of SPV technology and their use in grid-connected systems suggest that SPVs are here to stay are a viable option

for producing eco-friendly electricity for a variety of applications [1]. The Maximum Power Point tracking (MPPT) setting is used when an SPV system is connected to the grid in order to run the system and supply the most power to the grid [2]. Water pumps in the irrigation sector as well as the home and industrial sectors have profited from the usage of renewable energy-based power production in these sectors, especially in distant places. Additionally, PV electricity for water pumps has advantages such as low maintenance needs, easy installation, high dependability, silent operation, and less wear and tear due to the lack of moving components [3]. The MPPT algorithm with a dc-dc converter, the solar panel's maximum power is drawn. These algorithms range in complexity, responsiveness, and efficiency [4-5]. [6] Discusses possible application fields and offers a comprehensive analysis of solutions created especially for salient-pole PMSM. A promising application for sensorless control is interior PMSM (IPMSM) applications with highly saturated, high power densities. Applications with complex operational requirements and a wide range of parameter variations. [7] Model-based active flux observers with careful examination showed high potential. Additionally, the demonstration and discussion of the significant simplifications made possible by the use of active flux and the universality of machine topology. The sections that follow provide descriptions of the two primary kinds of rotor position estimate methods for PMSM. One approach is employing the PMSM salient pole features and high-frequency signal injection.When high-frequency sinusoidal or square wave impulses are injecting information about the rotor's position into the static coordinate system or the dq synchronous rotating coordinate system causes a high-frequency current to flow through the stator windings. This information may be gathered and demodulated to approximate the rotor position [8]. It is also practical to apply additional flux model-based approaches. The flux model, which takes into

consideration the stator voltage and current, establishes the rotor position [9]. Delay, angle estimate error, sampling circuit error, nonlinear inverter error and the temperature variation in the rotor resistor are some of the elements that can easily influence the flux model. Model reference adaptive control is known by the acronym MRAC [10]. In contrast to the adjustable model, the expectation model's equation contains no unknown parameters. Enhancement of the Kalman filter it's the perfect observer according to the minimal error covariance theory. Accurate system observation is still possible even in the presence of measurement and system noise by continuously modifying the gain matrix [11].Position and speed measurements are made by a phase-locked loop (PLL). A quadrature current model and the direct current model-based reluctance machine PLL estimator. The EMF and speed of a PMSM generator placed on the surface are calculated using a unique finite-position-set PLL. [12]– [14] At half-load, resistance to parameter modifications, and a notable decrease in oscillations. ANFIS a special kind of neuro-fuzzy architecture, has been widely used to describe or simulate a nonlinear system with the ultimate goal of learning-based fuzzy inference system explanation. The local linear input-output relations of adaptive systems can be represented by a set of fuzzy rules [15]. This paper proposes an ANFIS-SMO for Solar PV Array fed Encoder less PMSM Drive for Irrigation Applications. The organization of this paper is as follows. The introduction and literature review are covered in the first section. The system description is shown in Section-II, and the controlling topology and its suggested topology are described in Section-III.
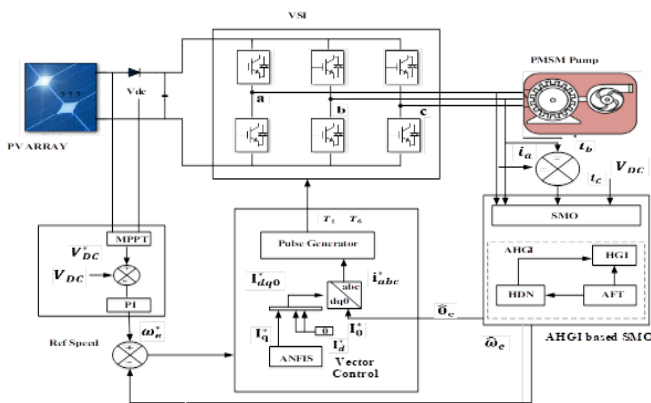
II. DESCRIPTION OF THE SYSTEM

Fig. 1 Proposed Architecture in Matlab/Simulink

The adaptive Neuro-Fuzzy interface system Figure 1 above provides a description of the based SMO for Solar PV Array fed Encoder less PMSM Drive. In this the supply to the PMSM drive considered from a primary source known as Solar. The PMSM requires AC power but the power from solar is in DC form. So an inverter is connected to convert DC power to AC power. The obtained AC power is then given to the PMSM drive. It is operated by using Field oriented Control (FOC) method. The inverter circuit is controlled by using AHGI based SMO technique is implemented. The obtained are given to the inverter through the PWM generator. The solar PV array is implemented by using the incremental conductance based MPPT technique.

Speed Control by using SMO based Encoder less Technique:

This section discusses the problems with back EMF estimation for generating rotor position that is based on SMO.

A. Estimation of Back EMF by using SMO:

In the PMSM, iron losses and magnetic saturation are not considered αβ-reference frame model, which assumes that the α-axis is parallel to phase-a and that it is electrically ahead of it by 90 degrees in β-axis.

$$V_\alpha = Lpi_\alpha + Ri_\alpha + e_\alpha \tag{1}$$
$$V_\beta = Lpi_\beta + Ri_\beta + e_\beta \tag{2}$$

L and R stand for, the phase's windings' inductance and resistance, respectively I_α, I_β, V_α, V_β, and e_α, e_β denote the voltage, current, and back-EMF components are each -reference frame-specific. The letter P represents a D/dt derivative operation. Figure 2 illustrates the association between the rotor fluxes and the back EMF elements. Consequently, e and e are derived from,

$$e_\alpha = -\lambda_{PM}\omega_e \sin\theta_e \tag{3}$$
$$e_\beta = -\lambda_{PM}\omega_e \cos\theta_e \tag{4}$$

Where the symbols for the permanent magnet's Flux linkage, rotor speed, and rotor angle are, respectively, ωe, θe, and λPM. (1) And (2) state that the SMO is destined to,

$$p\hat{\imath_\alpha} = L^{-1}R\hat{\imath_\alpha} + L^{-1}(v_\alpha - \hat{e}_\alpha) \tag{5}$$
$$p\hat{\imath_\beta} = L^{-1}R\hat{\imath_\beta} + L^{-1}(v_\beta - \hat{e}_\beta) \tag{6}$$

And,

$$\hat{e}_\alpha = k.sign(\hat{\imath}_\alpha - i_\alpha) = k.sign(\Delta i_\alpha) \tag{7}$$
$$\hat{e}_\beta = k.sign(\hat{\imath}_\beta - i_\beta) = k.sign(\Delta i_\beta) \tag{8}$$

Where '^' displays the predicted parameters; k is the gain; $\Delta i\alpha = \hat{\imath}\alpha - i\alpha$ and $\Delta i\beta = \hat{\imath}\beta - i\beta$ are present mistakes the signum function, in comparison, is represented by the following symbols: Sign (Δi_α)

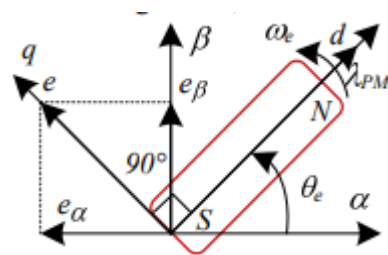$$= \begin{cases} +1, \Delta i_\alpha > 0 \\ -1 \Delta i_\alpha \leq 0 \end{cases} \tag{9}$$

Fig. 2 Vector Representation

The sliding surface, $\sigma\alpha\beta$ is defined as $\sigma\alpha\beta = \hat{\imath}\alpha\beta - i\alpha\beta = \Delta i\alpha\beta$ where $\sigma\alpha\beta = [\sigma\alpha \sigma\beta]T, \hat{\imath}\alpha\beta = [\hat{\imath}\alpha \hat{\imath}\beta]T, i\alpha\beta = [i\alpha i\beta]T$ and $\Delta i\alpha\beta = [\Delta i\alpha \Delta i\beta]T$. When sliding surface's present mistakes are visible, sliding surface becomes σαβ = 0, which results in $\hat{\imath}\alpha = i\alpha$ and $\hat{\imath}\beta = i\beta$.

From (3)–(4) and (7)–(8), it is clear that sign (Δiα) and sign I(Δiβ) both contain information on the rotor angle. Therefore, by estimating the back-EMF, the rotor angle can be found. S1 to S6 are the voltage source inverters, while VDC is the DC link voltage (VSI) switching states, and $iabc = [ia\ ib\ ic]$ are shown in Figure 3 as an example of the SMO-based back-EMF assessment. The stage PMSM flows and voltages are T and $vabc = [va\ vb\ vc]\ ê = [êf, êf]$ and T. T is a representation of the estimated back-fundamental EMF.
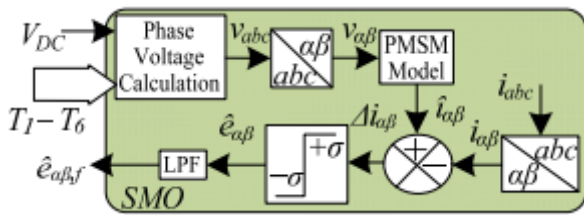
Fig.3. Controlling topology of SMO

Generation position of rotor at post process on the basis of Back EMF:

The prominent harmonics in the calculated fundamental back-EMF are 3rd, 5th, and 7th order ones can be found. With reference to Fig. 4, this paragraph analyses the applicability of LPF, SOGI, and FOGI for fundamental estimate as well as the results. The transfer function of the LPF, where c is the filter cut-off frequency, is GLPF $=[\omega c / (j\omega + \omega c)]$. Figures 4(a) and 4(b) display, respectively, the block diagram of the LPF and related Bode curves for ωc=314 rad/s (d). The basic back-EMF components' phase shift and attenuation caused by the LPF are depicted in the figure. These values at ωc=314 rad/s are determined from Fig. 4 to be 5 dB and 45°, respectively.

$$(d).\hat{\theta}_e = \tan^{-1}\left(\frac{\hat{e}_{\beta f}}{\hat{e}_{af}}\right) \qquad (10)$$

In relation to the SOGI quantities on the α-axis in Figure the transfer functions for in-phase (IS) and quadrature (QS) are obtained from 4(b) as [17],

$$I_S = \frac{\hat{e}_{af}}{\hat{e}_\alpha} = \frac{jk_1\omega_c\omega}{-\omega^2 + jk_1\omega_c\omega + \omega_c^2} \qquad (11)$$

$$Q_S = \frac{q\hat{e}_{af}}{\hat{e}_\alpha} = \frac{jk_1\omega_c^2}{-\omega^2 + jk_1\omega_c\omega + \omega_c^2} \qquad (12)$$

qêf is the primary quadrature part of ê, while k1 is the damping constant, which is typically set at 0.707 in consideration of convergence speed and stability margins. Figure 4 illustrates how SOGI-based filtering provides unity gain, greater high frequency, improved DC offset rejection, and no phase shift harmonic attenuation than LPF (e). However, it responds differently depending on inter-harmonics.

In Fig. 4, the FOGI is displayed (c). This leads to the creation of the following transfer functions for its quadrature (QF) and in-phase (IF)

$$I_F = \frac{\hat{e}_{af}}{\hat{e}_\alpha} = \frac{-k_2 k_3 \omega^2 \omega_c^2}{-k_2 k_3 \omega_c^2 \omega^2 + (-\omega^2 + jk_3\omega_c\omega + \omega_c^2)(-\omega^2 + \omega_c^2)} \qquad (13)$$

$$Q_F = \frac{\widehat{q}e_{af}}{\hat{e}_\alpha} = \frac{-k_2 k_3 \omega^2 \omega_c^3}{-k_2 k_3 \omega_c^2 \omega^2 + (-\omega^2 + jk_3\omega_c\omega + \omega_c^2)(-\omega^2 + \omega_c^2)} \qquad (14)$$

k2, k3, which stand for FOGI gains, are set to 1.5 and 3.1, respectively, for stability and fundamental filtering reasons. The FOGI's Bode diagrams, which are displayed in Fig. 4(f), unmistakably demonstrate that it outperforms SOGI's LOH rejection and high frequency attenuation capabilities. Additionally, it offers better inter-harmonic weakening due because it attenuates more quickly than SOGI. However, it is not possible to eliminate DLOH in a prudent and selective manner.
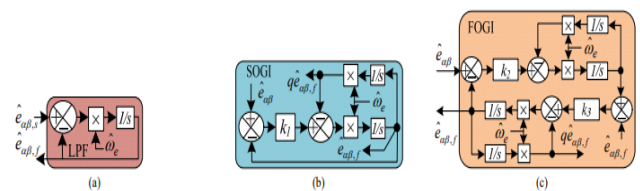

Figure-4: Controlling topology employed to estimate back emf

The aforementioned GIs do not record changes in cut-off frequency, either. We offer updated GIs with adaptive properties that are based on phase-locked loops (PLLs). However, because of the limited range that their frequency tracking covers, they are not suitable in solar WP systems for wide-range frequency tracking.

AHGI BASED SMO WAS DEVELOPED FOR PMSM ENCODERLESS OPERATION:

In order to simultaneously take advantage of the benefits and get around the shortcomings of the two GIs mentioned above, this section introduces an AHGI structure with decent high frequency attenuation and LOH elimination. The designed AHGI, the combination of an adaptive frequency tracker (AFT) with a hybrid generalised integrator (HGI). The HGI is the throbbing heart of the evolving AHGI structure. This procedure is divided into four steps. Due to its efficient band-pass filtering capabilities, SOGI is used in the subsequent stages, whereas FOGI is used in the initial stage due to its efficient filtering capabilities. In initial stage calculate fundamental back EMF voltage and remaining stages eliminates odd harmonics (3, 5 and 7).Here the signals pass through HDN to separate fundamental and harmonic signals from generated signal. Here first signal produce fundamental component and remaining signals produce to eliminate odd harmonics. The HGI receive four signal in a proper sequence. The HGI thus produces the fundamental component as well as the third, fifth, and seventh harmonics at the appropriate moments. By employing combination of HGI and HDN removes low order harmonics in the generated voltage. Therefore, as shown in Fig. 5, we may deduce that HGI and HDN collaborate to achieve selective harmonic removal.
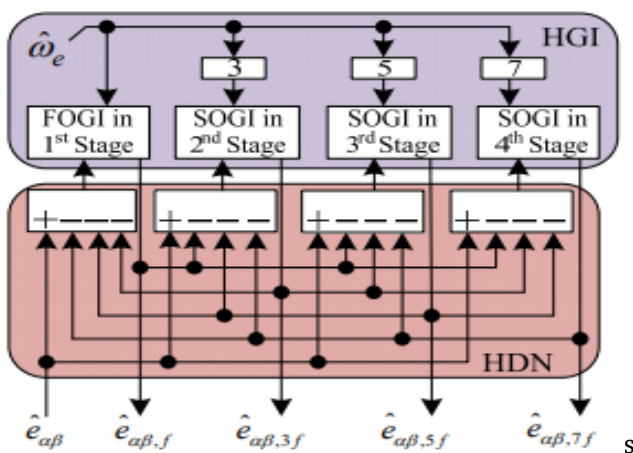
Fig. 5 Employed HGI and HDN for estimating Fundamental and DLOH

From Fig. 5, the closed loop transfer functions (TF) for in phase (I) and quadrature (Q) are derived as,

$$I = \frac{\widehat{e_{af}}}{\hat{e}_a} = I_F\{\prod_{k=3,5,7} \frac{1-I_{ks}}{1-I_F I_{kS}}\} \qquad (15)$$

$$Q = \frac{q\widehat{e_{af}}}{\hat{e}_a} = Q_F\{\prod_{k=3,5,7} \frac{1-Q_{ks}}{1-Q_F Q_{kS}}\} \qquad (16)$$

For k = 3, 5, 7, IkS and QkS are the in-phase and quadrature TF of the kth stage SOGI, respectively. The in-phase open-loop (OL) TF is calculated from (15) as follows:

$$I_{OL} = \frac{I}{1-I} = \frac{k_{OL}\prod_{j=1}^{12}(s+z_j)}{\prod_{i=1}^{14}(s+p_i)} \qquad (17)$$

Where pi, I are the OL poles, kOL = K2, zj, j = 1, 2...12 are the OL poles, and zj, j are the OL zeros. The OL gain is determined by k3/10 and is 0.46 for K2 = 1.5 and k3 = 3.1. According to Fig. 6, the Bode curves are generated using (17). Figures 6(a) and 6(b) display the phase-angle and magnitude plots at two frequencies, 100 and 314 rad/sec (b). T The phase-margin (PM) and gain-margin of the two operational frequencies (GM) are +180° and +21 dB, respectively. The AHGI has sufficient positive stability margins and good relative stability as a result. When c is equal to 314 rad/s, the gain-crossover frequency (gc) is 314 rad/s, and when c is equal to 100 rad/s, it is 100 rad/s. In Fig. 6, It is clear that the attenuation diminishes while the fundamental component loses unity rate for the high frequency components is 40 dB/decade. The three LOHs in the illustration, which show a substantial attenuation, demonstrate the selective harmonic removal. There is no phase shift in the fundamental frequency component either. With attenuations of - 95 dB and -83 dB for 314 rad/sec and 100 rad/sec, respectively, at 1 Hz, the figure shows that the AHGI even has strong DC offset rejection.

$$\widehat{\omega}_e = \frac{\hat{e}_{af}.p\hat{e}_{\beta f} - p\hat{e}_{af}.\hat{e}_{\beta f}}{(\hat{e}_{af}^2 + \hat{e}_{\beta f}^2)} \qquad (18)$$

The structure of AFT is depicted in Fig. 7(a). Calculations are made to determine the predicted back EMF components' dynamic frequency. Because of the fluctuating sun irradiation, frequency is

dynamic. Next, the estimated frequency is passed on to the HGI.
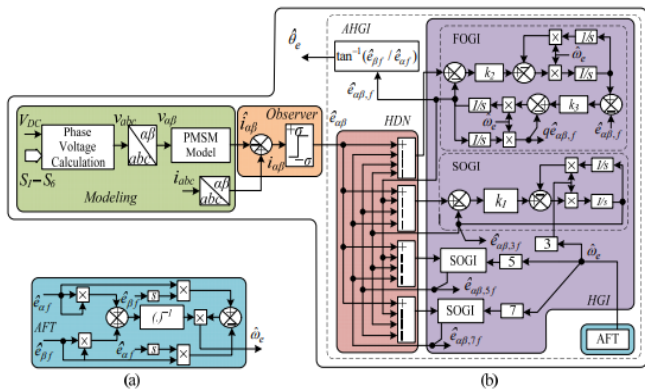

Figure 6 Proposed control topology

The block diagram of the SMO that uses AHGI to estimate the rotor angle is shown in Fig. 7(b). The PMSM's phase voltages are calculated as [4], where $\hat{v}abc = [\hat{v}a\ \hat{v}b\ \hat{v}c]\ T$.

$$\hat{V}_a = \{V_{DC}(2T_1 - T_3 - T_5)\}/3 \qquad (19)$$
$$\hat{V}_b = \{V_{DC}(-T_1 + 2T_3 - T_5)\}/3 \qquad (20)$$
$$\hat{V}_c = \{V_{DC}(-T_1 - T_3 + 2T_5)\}/3 \qquad (21)$$

From (1) and the figure, the estimated -components of current are derived (2) SMO uses the current error to estimate the back EMF of the αβ-axes. The DLOH is effectively removed by the AHGI, and it also removes the phase-shift and fundamental attenuation while adaptively tracking back the EMF frequency. As a result, it offers a reliable estimation of the basic back-EMF components. As a result, the rotor angle that is produced is precise. The ability to estimate back EMF for operation with and without harmonics now demonstrates the developed AHGI's advantage over LPF, SOGI, and FOGI. The results of the compared simulation are shown in Figures 8 and 9. It should be noted that new and old harmonic approaches operate better when the seventh, fifth, and third harmonics are present.

Proposed ANFIS based Controlling Topology:

Combination of fuzzy-Neuron networks (NN) are called as an ANFIS. The combined advantages of both

the systems produce best solution for non-linear stability improvement systems. With the capacity to learn and approximation nonlinear functions, its inference system resembles a set of IF-THEN fuzzy rules. ANFIS is viewed as a global estimator as a result. To use the ANFIS more effectively and efficiently, the best parameters determined by a genetic algorithm can be applied.
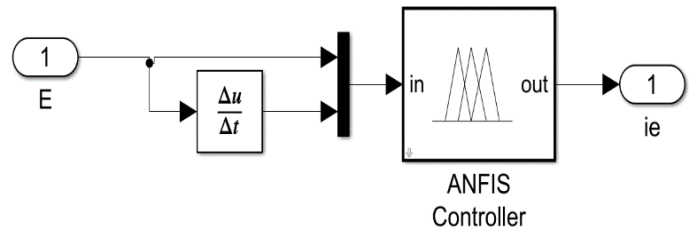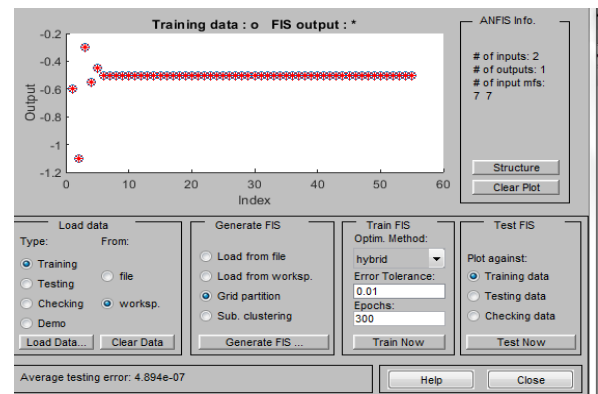

Figure 7 : Structure of ANFIS
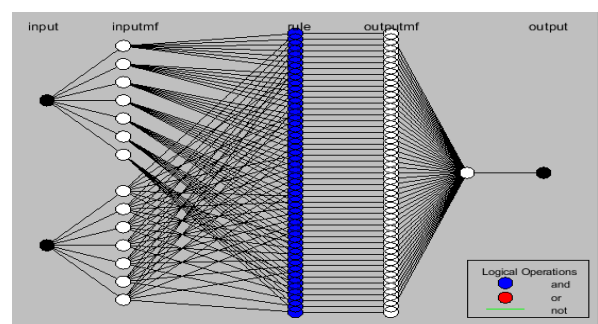

Figure 8 : ANFIS membership functions

Figure 9 : ANFIS Process

In this proposed work, an ANFIS Controller is implemented in the place of PI controller. Speed and reference speed is given as inputs to regulate the current. So, that Iq* is obtained. The basic structure of

ANFIS controller is depicted in above figure- . The error and change in error is shown in figure-1.

III. SIMULATION BASED RESULTS

This section describes the evaluation of simulation based results. For evaluating the performance of both convention topology and proposed topology Matlab/Simulink 2018a Software is used. This related assumed parameters are given below.

Table 1 : System Parameters

Parameters	Value	Units
PV array power (P$_{PV}$)	2.35	Kilo-watts
PV array voltage (V$_{pv}$)	413	Volts
PV array Voltage at open circuit (VOC)	480	Volts
PV array current (I$_{pv}$)	5.7	Amps
PV array current at short current (SOC)	6.0	Amps
Rotor mechanical torque of the motor (T$_r$)	14.01	Newton-meter
Motor power (P$_r$)	2.2	Kilo-watts
Motor speed (ωrm)	157	RPS
No of poles (p)	4	
Resistance of the motor (R$_{ph}$)	1.5	Ohm's
Inductance of the motor (L$_{ph}$)	3.5	Henry's
Torque constant of motor (K$_T$)	1.6	Nm/Arms
Voltage constant of motor (K$_V$)	68	Vrms/krpm
Voltage assumed to turn on the circuit (VS)	600	Volts
Current assumed to turn on the circuit (I$_S$)	30	Amps

a) Simulation Results attained by using PI Controller:
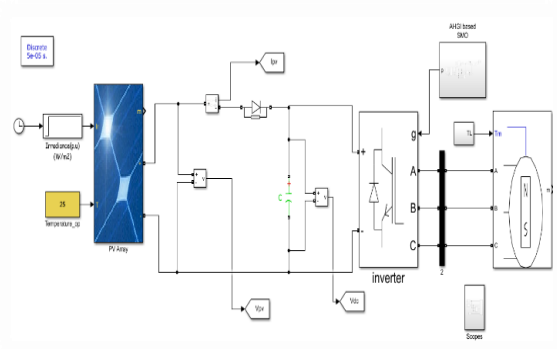
Figure 10: Simulink model of PI controlled AHGI based SMO system

The above figure will depicts about the simulink model of Conventional method. In this PI controller is implemented to generate the pulses to the inverter circuit. This related simulation results are depicted below.
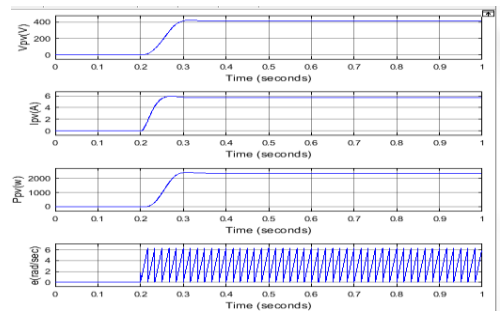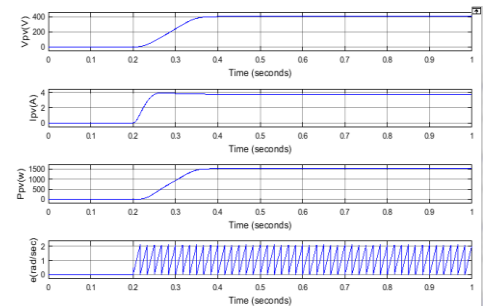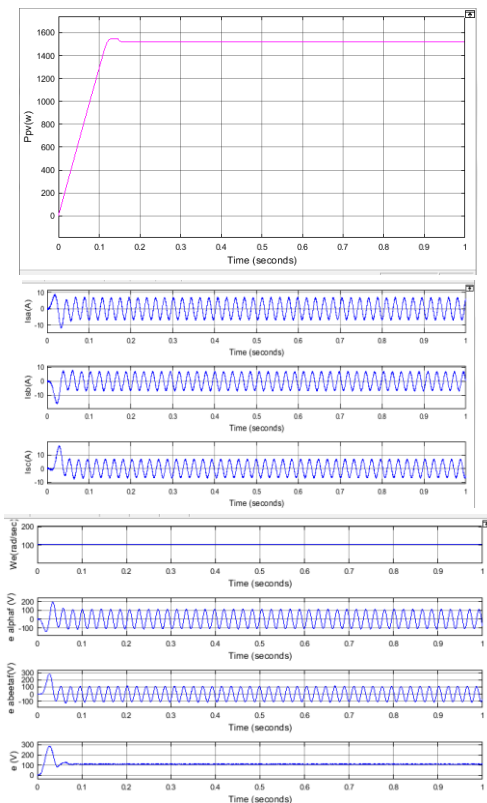

(a)Vpv, Ipv, Ppv and e at initial 1000W/m2 stage
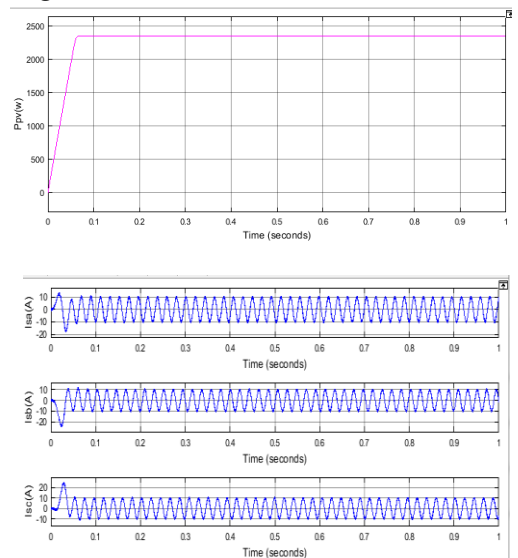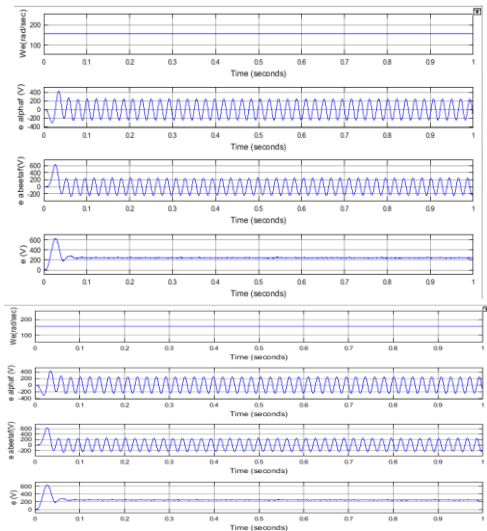
(b)Ppv, Isa, Isb, Isc, We, e alpha, e beeta, and e at initial 500 W/m2 stage.

(c)Vpv, Ipv, Ppv, e at Continuous 1000 W/m2 stage

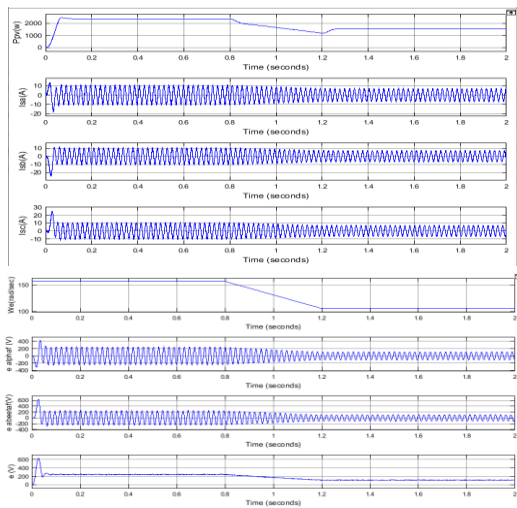(d)Ppv, Isa, Isb, Isc, We, e alpha, e beeta, e at continuous 500 W/m2 stage

Figure 11: Simulation results related to proposed system under steady state condition

The above figures will depicts about the grid, inverter and PMSM related simulation at steady state. This results are obtained by considering irradiance value as 1KW/m² and back emf. Although the two irradiation values are considered, the motor currents and back emfs are in the form of sinusoidal which evaluates the employed AHGI structure. But the current components has some harmonic distortions.
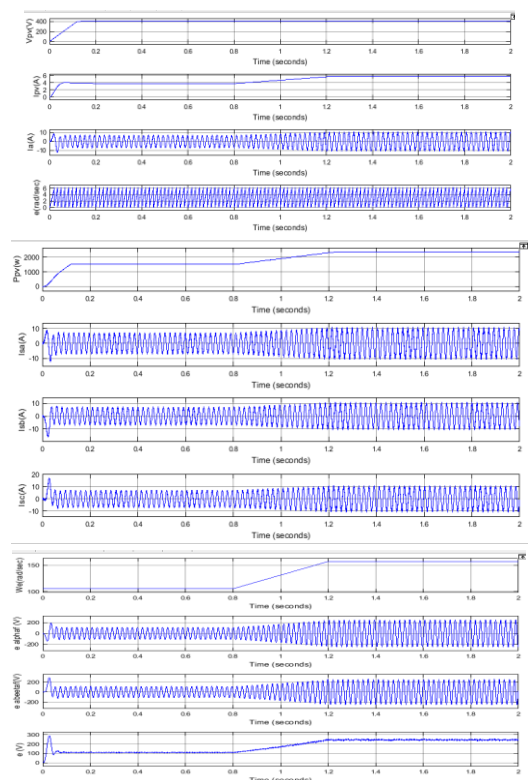
(e) Ppv, Isa, Isb, Isc, We, e alpha, e beeta, e from 500 W/m2 to 1000 W/m2
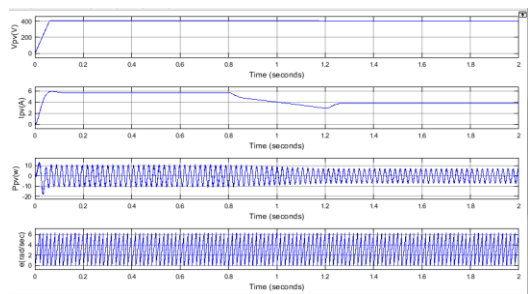
(f) Ppv, Isa, Isb, Isc, We, e alpha, e beeta, e from 1000 W/m2 to 500 W/m2

Fig. 12 Simulation results related to proposed system under dynamic state condition

The above figure will depicts about the simulation results obtained at dynamic state of the system. In this the performance of the system is examined at change in irradiation conditions (i.e.., 500-1000w/m²). This change in irradiation will leads to little decrease in current and raise in voltage related to PV can be observed. Although these changes are occurred but the system performs the stable operation.
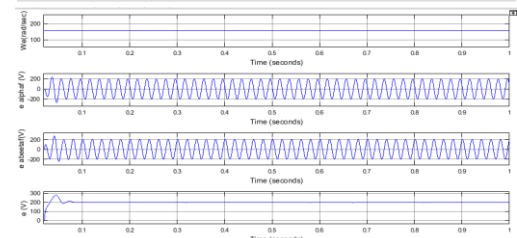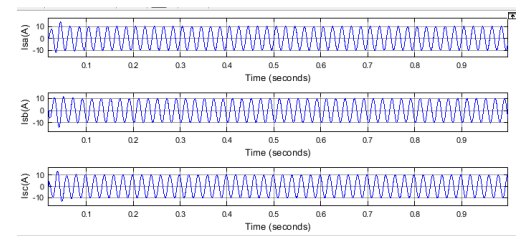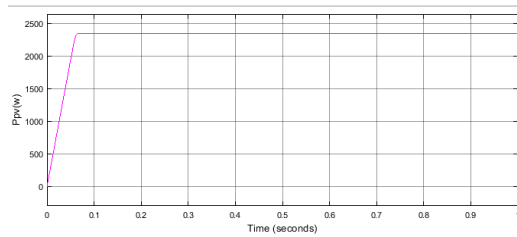
ANFIS Based Simulation Results:
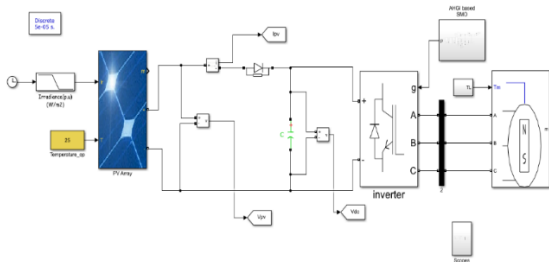
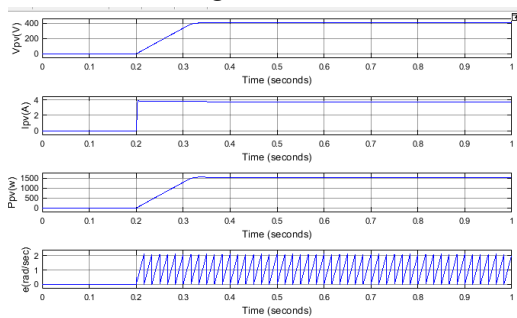Figure 13: Simulink Model of ANFIS based System

The above figure will depicts about the simulink model of proposed method. In this ANFIS controller is implemented to generate the pulses to the inverter circuit. This related simulation results are depicted below.
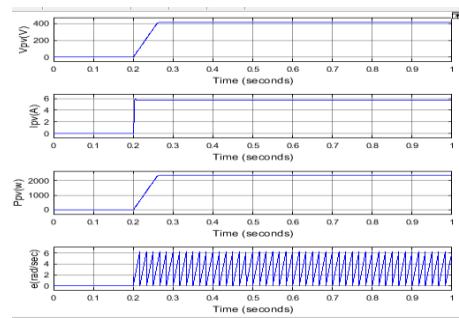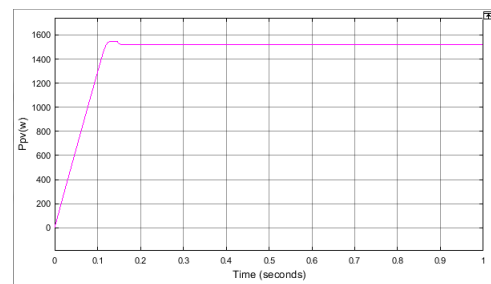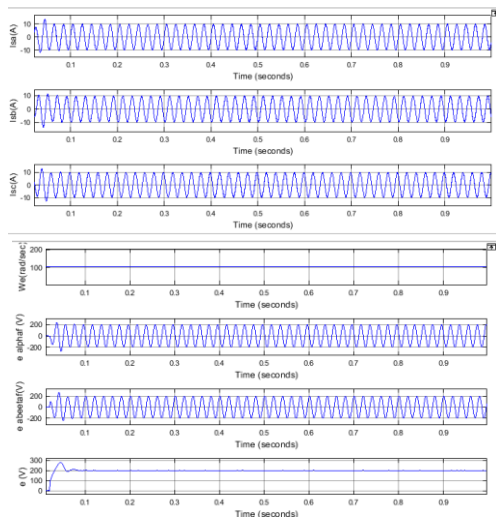

(g)Vpv, Ipv, Ppv, e at Continuous 1000 W/m2 stage

(b) Starting at 500 W/m2, (c),

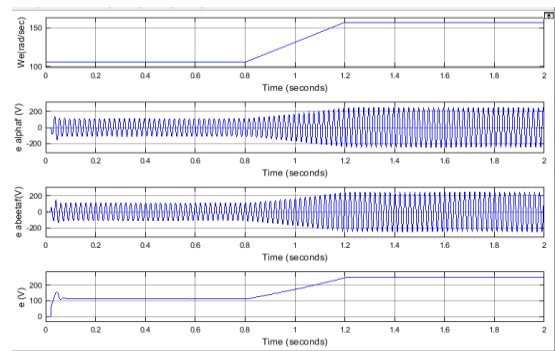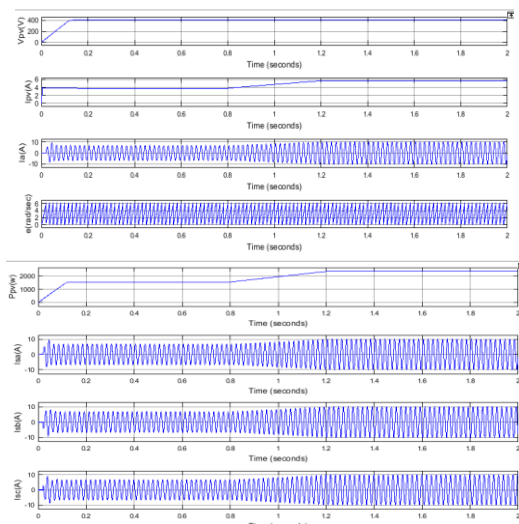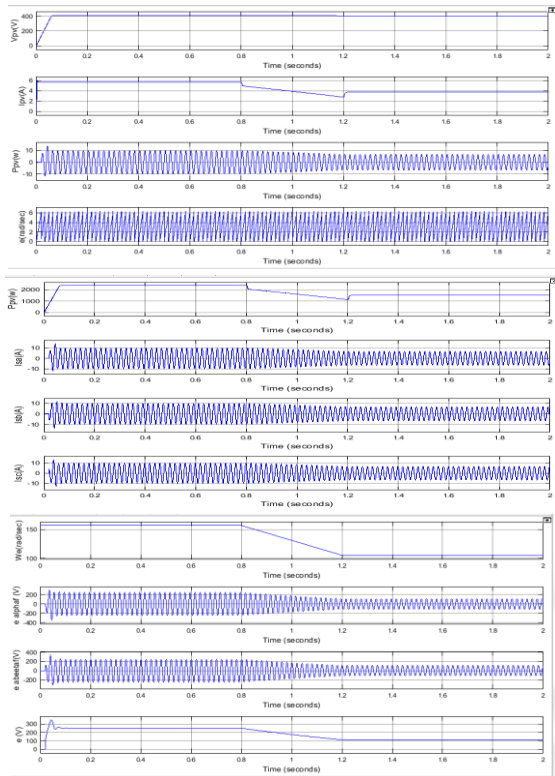(h) Ppv, Isa, Isb, Isc, We, e alpha, e beeta, and e, at Continuous 1000 W/m2,

(i)Ppv, Isa, Isb, Isc, We, e alpha, e beeta, and e, continuous running at 500 W/m2

Figure 14: Simulation results related to proposed system under steady state condition with ANFIS

The above figures will depicts about the grid, inverter and PMSM related simulation at steady state. This results are obtained by considering irradiance value as 1KW/m² and back emf. Although the two irradiation values are considered, the motor currents and back emfs are in the form of sinusoidal which evaluates the employed AHGI structure. In this the THDs in the current value are become lesser when compared to the conventional method.

(j)Ppv, Isa, Isb, Isc, We, e alpha, e beeta, and e, from 500 W/m2 to 1000 W/m2;

(K)Ppv, Isa, Isb, Isc, We, e alpha, e beeta, and e, from 1000 W/m2 to 500 W/m2

Fig. 15 Simulation result related to dynamic performance

The above figure will depicts about the simulation results obtained at dynamic state of the system. In the controlling topology of the system ANFIS Controller is employed. In this the performance of the system is examined at change in irradiation conditions (i.e.., 500-1000w/m²).This change in irradiation will leads to little decrease in current and raise in voltage related to PV can be observed. Although these changes are occurred but the system performs the stable operation.

Table 2: Comparison of Current THDs

Current	THD obtained by using PI Controller	THD obtained by using ANFIS Controller
Current THD obtained starting irr=500w/m²	12.06%	1.96%
Current thd continuous running at 500 W/m²	11.59%	2.94%
CURRENT THD Obtained at dynamic performance of the system	9.57%	1.68%
Current thd obtained at Variable irradiation condition(1000-500 and 500-1000 W/m²)	10.97%	1.03%

The above table-2 will describes the comparison of Current THDs by using both conventional and proposed topology. Among these two topologies, the proposed topology has less no. of THDs in current. So, the good power quality has been attained in the system.

IV. CONCLUSION

In this work, the Adaptive Neuro-Fuzzy interface system based SMO for Solar PV Array fed Encoder less PMSM Drive for irrigation Applications is implemented. In this the AHGI based Sliding mode observer has been implemented for improving the performance of water pump system. The Power supply has been considered from the solar PV, but it has an output of DC. Usually the PMSM drive needs the AC supply. So, an inverter is placed for the power conversion process. In order to regulate the reference current through a PI controller, the speed and reference speed are taken into account. The reference current is then given to the pulse generator, which then pulses the inverter circuit. With the ANFIS controller, the PI controller has been replaced. It has been observed that the Proposed ANFIS controller has produced the better results than the PI controller. The total harmonic distortions has been reduced it can be seen in above table-2. The performance of the system has been improved by enhancing the good power quality in the system. The simulation based results are evaluated by using Matlab/Simulink 2018a Software.

V. REFERENCES

[1].   J. Parikh, K. Parikh, "Growing Pains: Meeting India's Energy Needs in the Face of Limited Fossil Fuels," IEEE Power Energy Mag., vol. 10, no. 3, pp. 59-66, June 2012.

[2].   R. Kadri, J. Gaubert, G. Champenois, "An Improved Maximum Power Point Tracking for Photovoltaic Grid-Connected Inverter Based on Voltage-Oriented Control," IEEE Trans. Ind. Electron., vol. 58, no. 1, pp. 66-75, Jan. 2011.

[3].   G. Carannante, C. Fraddanno, M. Pagano, and L. Piegari, "Experimental performance of MPPT algorithm for photovoltaic sources subject to inhomogeneous insolation," IEEE Trans. Ind. Electron., vol. 56, no. 11, pp. 4374–4380, Nov. 2009.

[4].   N. Kumar, I. Hussain, B. Singh, and B. K. Panigrahi, "Single sensor based MPPT for partially shaded solar photovoltaic by using human psychology optimisation algorithm," IET Gener., Transmiss. Distrib., vol. 11, no. 10, pp. 2562–2574, 2017.

[5].   Q. Zhu, X. Zhang, S. Li, C. Liu, and H. Ni, "Research and test of powerloop-based dynamic

multi-peak MPPT algorithm," IEEE Trans. Ind. Electron., vol. 63, no. 12, pp. 7349–7359, Dec. 2016.

[6]. S. K. Sul, Y. C. Kwon, and Y. Lee, "Sensorless control of ipmsm for last 10 years and next 5 years," CES Transactions on Electrical Machines and Systems, vol. 1, no. 2, pp. 91–99, 2017.

[7]. I. Boldea and S. C. Agarlita, "The active flux concept for motionsensorless unified ac drives: A review," in International Aegean Conference on Electrical Machines and Power Electronics and Electromotion, Joint Conference, Sept 2011, pp. 1–16.

[8]. S. Yang, S. Yang and J.H. Hu, "Design consideration on the squarewave voltage injection for sensorless drive of interior permanentmagnet machines," IEEE Trans. Ind. Electron., vol. 64, no. 1, pp. 159- 168, Jan. 2017.

[9]. J. Holtz and J. Quan, "Drift- and parameter-compensated flux estimator for persistent zero-stator-frequency operation of sensorless-controlled induction motors," IEEE Trans. Ind. Appl., vol. 39, no. 4, pp. 1052- 1060, July-Aug. 2003.

[10]. F. Zhou, J. Yang and B. Li, "A novel speed observer based on parameter-optimized MRAS for PMSMs," in Proc.IEEE ICNSC, Sanya, 2008, pp. 1708-1713

[11]. Y. Shi, K. Sun, L. Huang and Y. Li, "Online identification of permanent magnet flux based on extended kalman filter for IPMSM drive with position sensorless control," IEEE Trans. Ind. Electron., vol. 59, no. 11, pp. 4169-4178, Nov. 2012.

[12]. M. H. Bierhoff, "A general PLL-type algorithm for speed sensorless control of electrical drives," IEEE Trans. Ind. Electron., vol. 64, no. 12, pp. 9253–9260, Dec. 2017.

[13]. M. Abdelrahem, C. M. Hackl, and R. Kennel, "Finite position set-phase locked loop for sensorless control of direct-driven permanent-magnet synchronous generators," IEEE Trans.

Power Electron., vol. 33, no. 4, pp. 3097–3105, Apr. 2018.

[14]. M. Fatu, C. Lascu, G. D. Andreescu, R. Teodorescu, F. Blaabjerg, and I. Boldea, "Voltage sags ride-trough of motion sensorless controlled PMSG for wind turbines," in Proc. 42nd IEEE Ind. Appl. Soc. Annu. Meeting, Sep. 2007, vol. 1, pp. 171–178.

[15]. N. Walia, H. Singh and A. Sharma, "ANFIS: Adaptive Neuro-Fuzzy Inference System- A Survey," International Journal of Computer Applications, vol. 123, no. 13, (2015), pp. 32-38.

Cite this article as :